33RD CONGRESS
OF THE INTERNATIONAL COUNCIL
OF THE AERONAUTICAL SCIENCES
STOCKHOLM, SWEDEN, 4–9 SEPTEMBER, 2022

ICAS 2022 SWEDEN

# LES of Combustion Dynamics in an Ethylene-Hydrogen-Air Ramjet

N. Zettervall[1], K. Nordin-Bates[1], C. Ibron[1] & C. Fureby[2]

[1]Swedish Defence Research Agency, FOI, Defence Security Systems Technology, SE 147 25 Tumba, Stockholm, Sweden
[2]Energy Sciences, Lund University, Box 118, SE 221 00, Lund, Sweden

## Abstract

A combustion Large Eddy Simulation (LES) is used to examine the flow, mixing, fuel-injection and combustion dynamics of a ramjet combustor with a cavity flame holder. The combustor is a running 50/50, in mole, ethylene/hydrogen fuel mixture. A direct-connect facility dual-mode ramjet/scramjet combustor presents the target case, with in the literature available experimental data is used in the present study for validation of the current LES results. Experimental data for time-averaged chemiluminescence, represented by the CH* signal, and CH-PLIF and OH-PLIF, are used to validate the LES. The LES, using a compact 66-step reaction mechanism for the ethylene/hydrogen/air combustion, predicts a highly dynamic combustion behavior, where the flame oscillates between longer sequences in a cavity stabilized state and shorter ones with a jet-wake stabilized state. A volume averaging in cross-section slabs along the combustor length, plotted over time, is used to further examine and visualize the dynamic combustion and the effects of the dynamics on the temperature, pressure, heat release and axial velocity. Such cross-section slabs, and constant volume simulations, is used to further investigate the predictive effect of the accumulation of $H_2O_2$ on the combustion dynamics and the sudden increases in flame size associated with the dynamic flame behavior.

**Keywords:** LES, ramjet, combustion dynamics, ethylene, hydrogen

## 1. Introduction and Background

Ramjet and scramjet engines have the potential to provide economical air-breathing propulsion at high Mach numbers, with possible areas of application including hypersonic cruise missiles, transportation and reusable launch vehicles [1]. Over the years, a large number of experimental and simulation studies have been carried out, with the majority using hydrogen as fuel. With the increase in knowledge of the combustion processes inside the engine, and with the practical difficulties of handling and storage involved when using hydrogen, a move towards hydrocarbon fuels is desirable. However, choosing hydrocarbons instead of hydrogen poses new challenges, with the longer ignition times of long-chained hydrocarbons being one of the most critical. This is an issue due to the short fuel-residence times in a ramjet or scramjet, which are often less than one millisecond [2], and can in turn cause problems with ignition of the fuel and flame anchoring. One approach for mitigation of the effects of the long ignition process associated with hydrocarbons is the dilution of the fuel mixture with hydrogen, effectively shortening the ignition delay time and increasing flame stability.

When considering hydrocarbon fuels, there are many attractive options purely from an ignition delay point of view. However, these do not always coincide with desirable practical characteristics regarding larger scale production and handling of these fuels. The likely best option from a practical point of view would be the use of commercially-available jet fuel, such as Jet A1 or JP-5, even though these are not the best-suited regarding ignition times. Nevertheless, various studies have been performed of a range of hydrocarbons for use in supersonic combustion, including pure ethylene ($C_2H_4$) [2-5], ethylene-hydrogen ($C_2H_4/H_2$) mixtures [6-9], ethylene-methane ($C_2H_4/CH_4$) mixtures [1,10,11], pure kerosene [12-16] and kerosene-hydrogen mixtures [17].

In this study, combustion Large Eddy Simulation (LES) [18,19] together with finite-rate chemistry using a reduced reaction mechanism is used to examine the subsonic cross-flow in a model ramjet combustor investigated experimentally by Micka et al. [6,7]. The experiments and simulations use a 50/50 $C_2H_4/H_2$ by volume fuel mixture, with a combustor inlet velocity of 468 m/s, or Ma 0.62, a typical ramjet flow speed. This study is an extension and continuation of a previous study on the same combustor set-up, but then using pure $H_2$ as fuel. [20,21].

Experimental data for the $C_2H_4/H_2$ case investigated here [6] include time-averaged CH* and OH* chemiluminescence from the jet flame, instantaneous and time-averaged CH-PLIF, and instantaneous PLIF images of OH and formaldehyde ($CH_2O$). Heat release rate distributions were estimated based on the OH* and CH* signals. Another similar study from the same authors [7] investigated the same combustor, at the same temperature condition, but with the addition of $H_2$ injected directly into the cavity of the combustor.

## 2. The University of Michigan Dual Mode Ramjet Experiments

The experiments [6,7] were carried out in the University of Michigan JICF supersonic combustion facility, shown in figure 1. A two-dimensional Ma 2.2 nozzle feeds a constant area isolator with a cross-section of 25.4 by 38.1 mm, which extends 358 mm upstream of the fuel jet. A rectangular cavity is located 44.5 mm downstream of the fuel jet, 50.8 mm long and 12.7 mm deep, and spanning the full width of the facility section. Behind the cavity, a 349 mm long 4° diverging combustor section begins, ending in a 152.0 mm diameter exhaust. Room temperature gaseous 50/50 $C_2H_4/H_2$ fuel was injected sonically through the single 2.49 mm diameter injection port on the centerline of the combustor. No pilot fuel injection inside the cavity was present in these experiments. Having pilot fuel injected in the cavity has been shown to significantly affect flame structures and stability properties [22-24], depending on where the cavity is fueled.

In order to achieve sufficient air stagnation temperatures of up to 1500 K, the inlet air was heated using both an electric heater and a $H_2$-fueled vitiated air heater. In the study simulated here, the stagnation temperature of 1470 K was close to the maximum possible in the facility. Additional oxygen ($O_2$) was added to the heated vitiated inlet air in order to keep the $O_2$ mole fraction at 0.21.

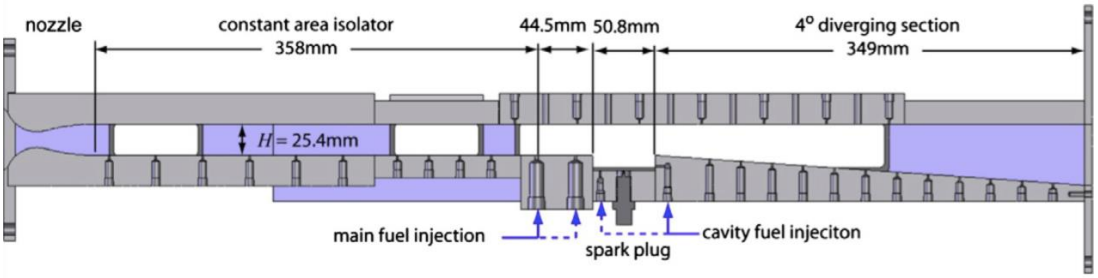


Figure 1 - Schematic of the University of Michigan supersonic combustion facility, from Micka et al. [6].

From the experimental studies [6,7], the stagnation pressure, stagnation temperature and nozzle throat Mach number, $p_0$, $T_0$ and $\mathrm{Ma}_0$, respectively, are provided. Assuming ideal gas in the nozzle section, the inflow static temperature, $T_{\mathrm{in}}$, can be computed from $T_0/T_{\mathrm{in}}=1+\frac{\gamma-1}{2}\mathrm{Ma}_0^2$, where $\gamma \approx 1.4$ for air. The inflow static pressure, $p_{\mathrm{in}}$, is similarly given by $p_0/p_{\mathrm{in}}=(1+\frac{\gamma-1}{2}\mathrm{Ma}_0^2)^{\gamma/(\gamma-1)}$. The inflow Mach number together with the speed of sound, $c=(\gamma RT)^{1/2}$, is used to obtain the inflow velocity, $v_{in}$. The fuel temperature and velocity, together with the global equivalence ratio, $\varphi$=0.42, are as provided in [6,7].

## 3. LES Models, Numerical Methods and Computational Set-Up

The flow in the compressible reactive system is modelled using LES, based on implicitly-filtered conservation equations for mass, momentum, energy and species masses [25]. The mixture is assumed to be composed of thermally-perfect gaseous species with individual formation enthalpies and linear specific heats. The mixture viscosity is modelled using Sutherland's law, while Fickian diffusion and Fourier heat conduction are incorporated assuming constant Prandtl number and species Schmidt numbers respectively. Species reaction rates are determined by summation over a system of reactions, each of which has a rate determined by Arrhenius-type rate laws.

The filtered equations are closed using the Smagorinsky model to estimate the subgrid stresses, while the filtered reaction rates are determined using the Partially Stirred Reactor model of [26]. The LES-PaSR model employed in this study has been widely used in combustion simulations, and is validated for laboratory combustors [27,28], afterburners [29], gas turbine combustors [30], as well as different scramjet combustors [31,32].

The LES-PaSR model equations are solved using a fully-explicit finite-volume code based on the OpenFOAM C++ library [33]. High-order monotonicity-preserving reconstruction of the convective fluxes and central differencing of the diffusive fluxes [34], are combined with a total variation diminishing based Runge-Kutta time integration scheme to result in a second-order accurate algorithm. The chemical source terms in the species conservation equations are evaluated using an operator-splitting approach together with a stiff Rosenbrock solver [35]. The code is density based, conservative, fully compressible, and stability is imposed using compact stencils and by enforcing conservation of kinetic energy with a Courant number limitation of 0.5.

The simulation domain starting at the Laval nozzle and ending at the exit of the combustor section. The operating conditions match those for the experiment [6,7] in terms of fuel, total pressure and temperature ($p_0$ and $T_0$), combustor inflow temperature, pressure, density and velocity ($T_{in}$, $p_{in}$, $\rho_{in}$, $v_{in}$), fuel temperature, velocity, equivalence ratio, total pressure, pressure and density ($T_{fuel}$, $v_{fuel}$, $\varphi$, $p_{0,fuel}$, $p_{fuel}$, $\rho_{fuel}$). The domain is discretized with a hexahedral mesh of 7.2 million cells having refinement at the walls. Dirichlet boundary conditions are used for all variables at the inlet and at the sonic injectors. At the outlet, zero Neumann conditions are used for all variables, since the combustor dumps in a large exhaust. In the combustor, a no-slip boundary condition is used for velocity, together with zero Neumann conditions for all other variables

## 4. $C_2H_4$-Air and $C_2H_4$-$H_2$-Air Combustion Chemistry

The $C_2H_4$-air and $C_2H_4$-$H_2$-air combustion is modelled using a 66-step reaction mechanism [36] that has previously been extensively validated against chemical kinetic experimental data as well as detailed reaction mechanisms [37-39] under pure $C_2H_4$-air conditions. The reduced mechanism consists of 23 species and 66 irreversible reactions and is here referred to as Z66. Because of its

considerably smaller size, and hence its lower computational cost compared to a detailed mechanism, a reduced mechanism is more suitable for finite-rate combustion LES. Several detailed mechanisms for ethylene combustion are available [37-39], consisting of 57 [38], 111 [39] and 253 [37] species, among 270 [38], 784 [39] and 1542 [37] reversible and irreversible reactions. Here all these three detailed mechanisms will be compared to Z66 when investigating the modelling performance. The detailed mechanisms will be referred to as the San Diego (SD) mechanism [38], the USC mechanism [39] and the Aramco mechanism [37].

The Z66 mechanism development starts with the selection of relevant chemical reactions and their corresponding rate parameters [36,40,41]. Experimental data and simulation results from detailed mechanisms then guide eventual adjustment of rate parameters. The mechanism build-up of Z66 follows previous work on propane [29] and kerosene [40], using a methodology where the mechanism is divided into three separate submechanisms: *fuel breakdown*, *intermediate hydrocarbon oxidation*, and *base mechanism*. This methodology has been extensively described for both ethylene [36] and kerosene [40]. The primary flame parameter targets for Z66, the so-called development targets, are the laminar burning velocity, $s_L$, flame temperatures, $T_{flame}$, major species concentrations and ignition delay times, $\tau_{ig}$, all for a wide range of equivalence ratios and initial gas temperatures and pressures.

Even though the Z66 mechanism development was initially aimed at simulations with pure $C_2H_4$-air mixtures, the detailed $H_2$-air chemistry on which the mechanism is based enables extensions to the inclusion of different amounts of $H_2$. No comparison of Z66 against $C_2H_4$-$H_2$-air mixtures has previously been presented, hence the following results section will not only present results for pure $C_2H_4$-air mixtures but $C_2H_4$-$H_2$-air mixtures as well. Because Z66 has previously been extensively validated, the following comparison will focus on laminar burning velocities and flame temperatures at standard conditions of T = 300 K and p = 1 atm, as well as ignition delay times for lean and stoichiometric mixtures at p = 1 and 10 atm. For a more thorough analysis of Z66, investigating more flame parameters at a wider set of conditions we refer to the original paper for Z66 [36].

Z66, and the propane and kerosene mechanisms on which it shares the same development methodology, have all previously been employed in combustion LES [29,42,43]. The highly reduced nature of these mechanisms together with their high predictability performances makes them ideal chemistry models for finite rate combustion LES.

## 4.1 Laminar Burning Velocity and Flame Temperature, $C_2H_4$-Air Mixtures

Laminar burning velocity simulations at standard conditions of p=1 atm and T=300 K are shown in Figure 2(a), and the maximum flame temperatures achieved at the same initial conditions are shown in Figure 2(b). For the laminar burning velocities, all mechanisms match the experimental data sets, with the exception of the SD mechanism at fuel lean conditions, where a slight overprediction is evident. For the flame temperatures, all mechanisms show similar values, and all show slightly lower values compared to the experimental data. The deviations between the mechanisms are small, and overall Z66 is in good agreement with the experimental data and the detailed mechanisms for both laminar burning velocities and maximum flame temperatures.

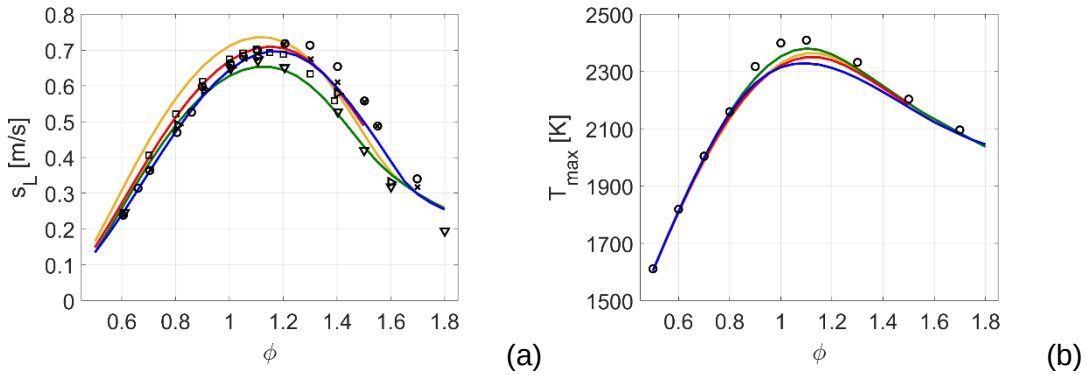


Figure 2 - (a) Laminar burning velocities and (b) flame temperature at standard conditions of 1 atm and 300 K for $C_2H_4$-air mixtures. Legend, experimental data: (a) ○– [44], **v** – [45], **x** – [46], **>** – [47], □ – [48]. (b) ○ – [49]. Simulations: Z66 - blue, Aramco - red, USC - green, SD – yellow.

## 4.2 Ignition Delay Time, $C_2H_4$-Air Mixtures

Ignition delay time simulations were performed at equivalence ratios of φ = 0.5 and 1.0, and pressures of 1 and 10 atm. Corresponding experimental data for the same equivalence ratios and pressures are shown in black symbols, and experimental data using slightly higher pressures (2-3 atm in Figure 3, and 15 atm in Figure 4) are shown in pink symbols. The range of simulated initial gas temperatures ranges from 910 K to 1430 K, showing the mechanism performances when transitioning from medium to high temperatures.

At 1 atm, Figures 3(a) and 3(b), Z66 shows good predictions of the experimental data by Kopp et al. [50]. Of the four mechanisms, it is mainly USC that differs, and at higher temperatures. The USC mechanism is however the only one matching the experimental data by Kalitan et al. [51]. The SD and Aramco mechanisms display a bending of the ignition curve when transitioning from medium to high temperatures, starting at around 1000 K, similar to the ignition behaviour seen in the crossover region for $H_2$-air ignition [52]. Overall, the predictions of Z66 are in line with the detailed mechanisms and the experimental data.

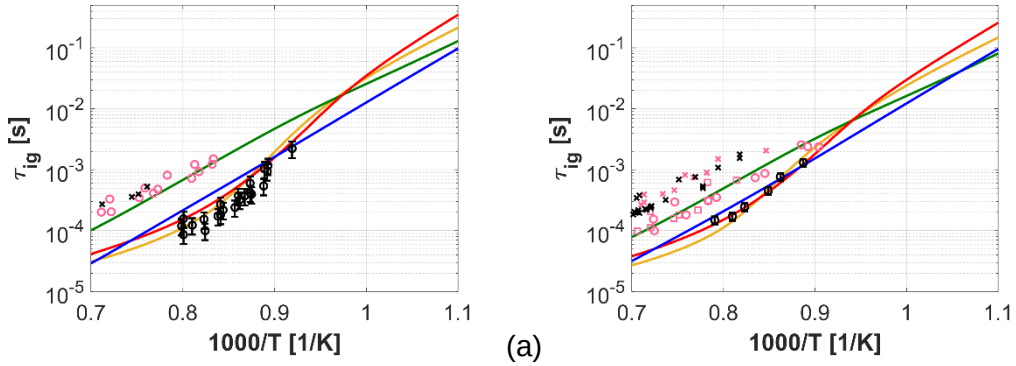


Figure 3 - Ignition delay time predictions of a $C_2H_4$-air mixture at p = 1 atm and (a) φ = 0.5 and (b) φ = 1.0. Legend, experiments: (a), black symbols: ○ – [50], **x** – [51]. Pink symbols: ○ – [48]. (b), black symbols: ○ – [50], **x** – [51]. Pink symbols: ○ – [53], **x** – [48], □ – [51]. Simulations: Z66 - blue, Aramco - red, USC - green, SD – yellow.

At elevated pressures of 10 atm, Figures 4(a) and 4(b), the overall ignition delay time decreases. Here Z66 give consistently slightly higher predictions than the detailed mechanisms, but it falls in between the present experimental data. Again the SD and Aramco mechanisms display a bent ignition curve similar to what is seen for $H_2$-air ignition, and at this elevated pressure the bending of the curve is shifted toward high temperatures compared to the 1 atm case above.

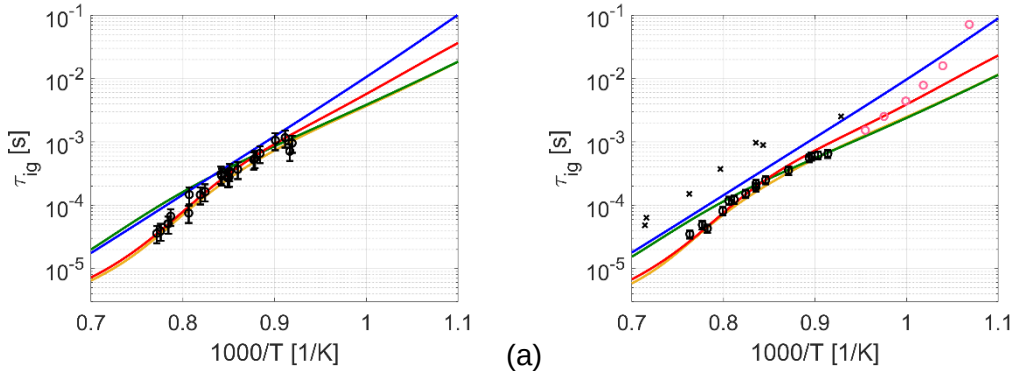


Figure 4 - Ignition delay time predictions of a $C_2H_4$-air mixture at p = 10 atm and (a) φ = 0.5 and (b) φ = 1.0. Legend, experiments: (a), black symbols: ○ – [50]. (b), black symbols: ○ – [50], **x** – [53]. Pink symbols: ○ – [54]. Simulations: Z66 - blue, Aramco - red, USC - green, SD – yellow.

## 4.3 Laminar Burning Velocity, $C_2H_4$-$H_2$-Air Mixtures

Due to a lack of experimental data for $C_2H_4$-$H_2$-air mixtures, Z66 will be compared solely against predictions by the detailed mechanisms. The three fuel fractions used in the simulated mixtures are 75/25 $C_2H_4$/$H_2$ and 50/50 $C_2H_4$/$H_2$, by mole. As expected, the laminar burning velocities increase with an increasing $H_2$ fraction, as the inherently faster burning velocity of $H_2$ is partly transferred into the new mixture compositions. The mechanisms respond to the increase in $H_2$ rather differently, and at

25% $H_2$ enrichment the velocity increase of the USC mechanism is far below that of the other three mechanisms. At 50% $H_2$ enrichment, differences are even greater, with Z66 and USC showing the highest and lowest values, respectively, and with SD and Aramco giving similar predictions. The curve shapes of the $C_2H_4$-air mixture in Figure 2(a) are however intact at both $C_2H_4/H_2$ mixture conditions, with the only difference being in the amplitudes. The inherently different curve shape of pure $H_2$-air, with considerably higher velocities at fuel rich conditions, is not present here suggesting that major chemical pathways are still maintained from the $C_2H_4$-air chemistry.

Without experimental data it is difficult to draw too certain conclusions, but overall Z66 predict similar trends as the detailed mechanisms, only with differences in amplitude, especially for the 50/50 fuel mixture.

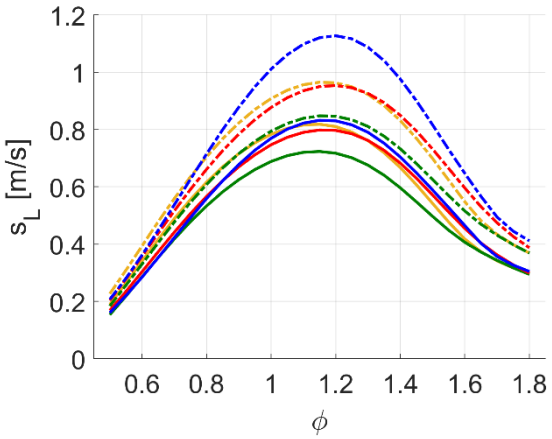


Figure 5 - Laminar burning velocities at standard conditions of 1 atm and 300 K for $C_2H_4$-$H_2$-air. 75/25 $C_2H_4/H_2$ – solid line, 50/50 $C_2H_4/H_2$ – dashed line. Legend: Z66 - blue, Aramco - red, USC - green, SD – yellow.

### 4.4 Ignition Delay Time, $C_2H_4$-$H_2$-Air Mixtures

As with the laminar burning velocity, a lack of experimental data for ignition delay times on $C_2H_4$-$H_2$-air mixtures means Z66 will be compared solely against predictions by the detailed mechanisms. Ignition delay time predictions for all four mechanisms, using $C_2H_4$-air and 50/50 $C_2H_4$-$H_2$-air mixtures, at φ = 1.0 at p = 1 atm and 10 atm, are shown in Figures 6(a) and 6(b), respectively. Here Z66 show a general decrease in ignition time when $H_2$ is added, whereas all three detailed mechanisms show a decrease at higher temperatures and an increase at medium temperatures. The USC mechanism also changes ignition curve shape compared to the pure $C_2H_4$-air mixture condition, producing a shape similar to the ones by the SD and Aramco mechanisms. With the inclusion of $H_2$ all detailed mechanisms get stronger bending of the ignition curve, resembling more closely the curve shape of the crossover region of a pure $H_2$-air mixture [52].

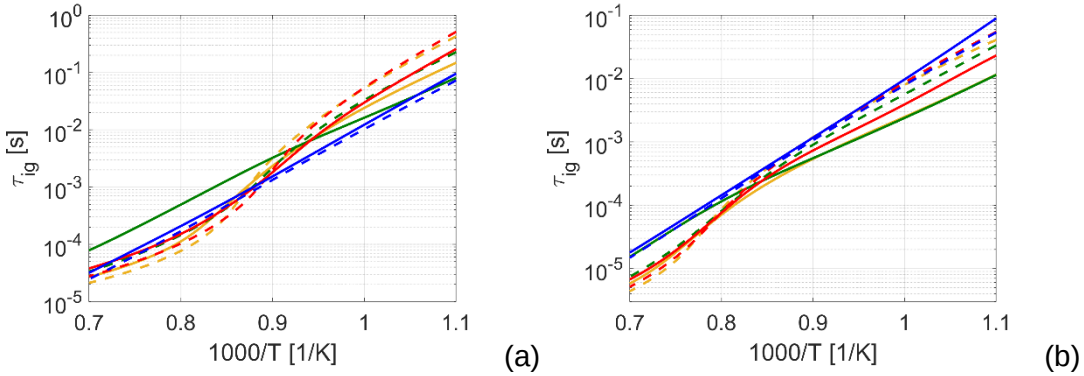


Figure 6 - Ignition delay time predictions of $C_2H_4$-air (solid lines) and 50/50 $C_2H_4$-$H_2$-air (dashed lines) mixtures at (a) φ = 1.0 and p = 1 atm and (b) φ = 1.0 and p = 10 atm. Legend: Z66 - blue, Aramco - red, USC - green, SD – yellow.

## 5. Results and discussion

In this section the results of the LES of the ramjet combustor will be presented and compared to available experimental data from the study by Micka et al. [6].

The supersonic air inflow (Ma = 2.2) is decelerated within the isolator section of the combustor to subsonic conditions (Ma = 0.62) at the point of fuel injection, with corresponding increases in the pressure and temperature. This occurs via a combination of a series of shock-waves and separation of the boundary layers from the isolator wall.

The fuel jet enters perpendicular to the mean-flow direction and is turned downstream by the bulk flow as it proceeds into the combustion chamber. The jet acts as an dynamic obstacle within the air-stream, resulting in a shock-wave upstream of the injector. The strong shear layers created between the fuel and air flows result in instabilities in the jet surface. These instabilities, coupled with the turbulent velocity fluctuations created upstream in the air-flow result in fuel-air mixing within this layer. The hot air ignites the resultant fuel-air mixture, with the resultant combustion releasing heat and the resultant volumetric expansion accelerating the flow to supersonic conditions downstream of the cavity.

The flow is illustrated in Figure 7 using representative instantaneous centre-plane plots of temperature, $T$, chemical heat release, $\dot{Q}$, Mach number, Ma, ethylene mass fraction, $Y_{C_2H_4}$, and numerical Schlieren. Aspects of the flow are seen to be highly dynamic, however, with for example the combustion location and extent and the isolator separation location varying periodically. This dynamic behaviour is investigated further in the following section.

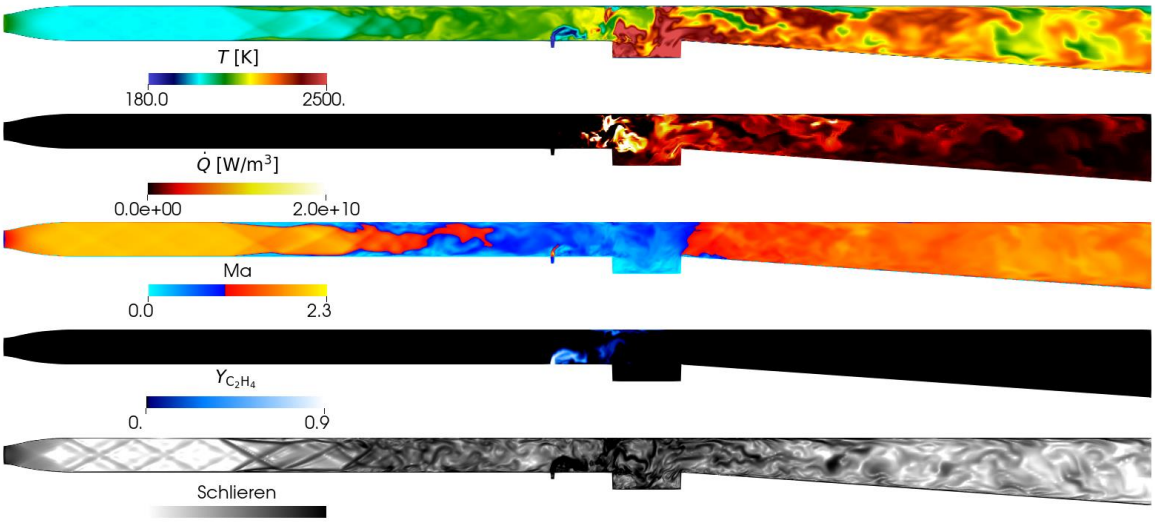


Figure 7 - Instantaneous center-plane plots of temperature, $T$, chemical heat release, $\dot{Q}$, Mach number, Ma, ethylene mass fraction, $Y_{C_2H_4}$, and numerical Schlieren.

## 5.1 Experimental Comparison

The time-averaged chemiluminescence from the flame are in the experiments represented by the CH* signal, shown in Figure 8(a). This can be approximated in the LES by the time-averaged CH mass fractions, Figure 8(b), integrated across the combustor width. The peak value from the experimental CH* signal is located above the the cavity at approximately one third of its length, whereas the time-averaged CH peak from the LES is located slightly further downstream. The LES results also appear to show low levels of CH created closer to the injector than seen in the experiment, though the range covered by the colour-map in the experimental plots is unclear. It should also be noted that CH* mainly occurs before CH in the combustion process and hence an upstream shift is expected.

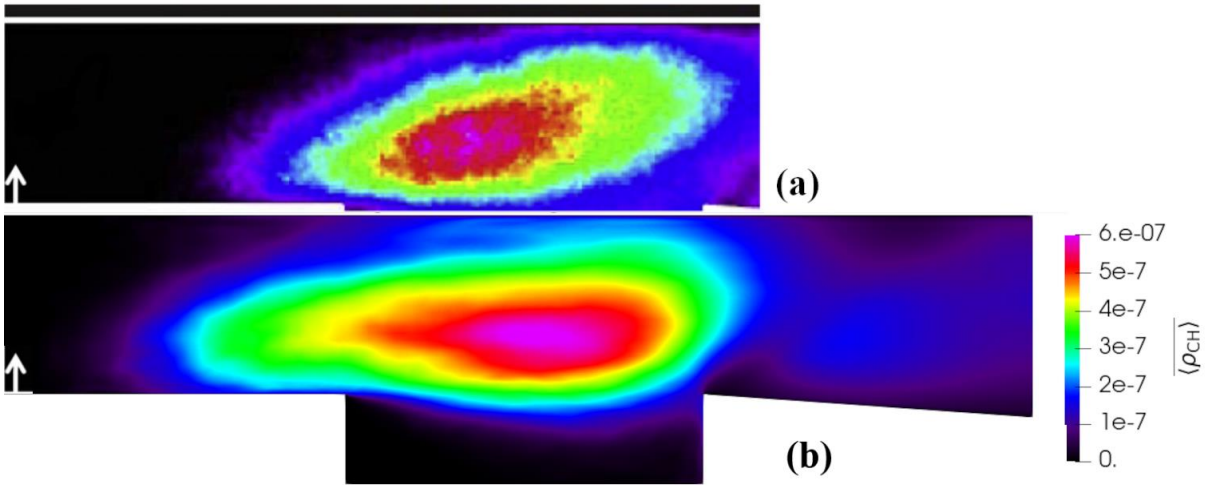


Figure 8 - Experimental time-averaged CH* chemiluminescence from the jet flame,from [6] (top), and time-averaged, line-of-sight averaged CH mass from LES (bottom).

When, instead of the CH* signal, one compares the measured time-averaged CH-PLIF signal from the experiments to the centre-plane CH densities from the LES, Figures 9(a) and 9(b), respectively, the similarities found in the previous plot are repeated in the area above the cavity. Further downstream, however, the experimental results suggest higher CH concentrations than those seen in the LES results. The experimental results are however generated from four separate frames and it is unclear from [6] whether the results in each of these are independently scaled.

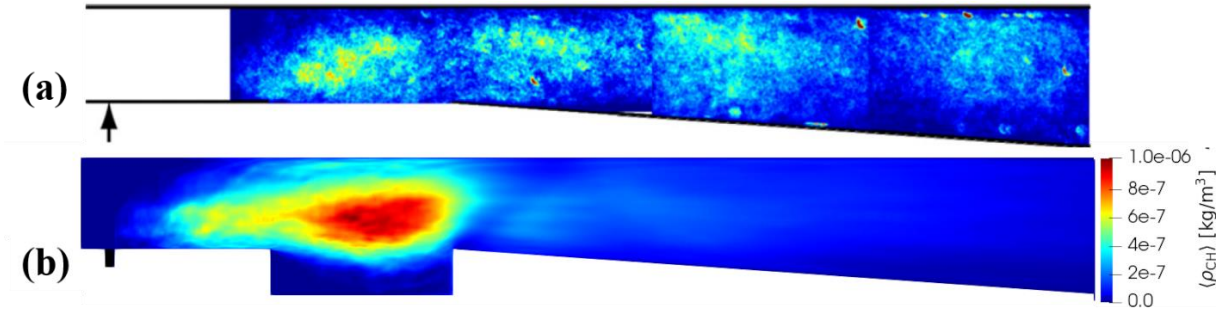


Figure 9 - Time-averaged centre-plane CH-PLIF signal from the experiments in (a) and time-averaged centre-plane CH density from the simulations in (b).

Figure 10 show a selection of instantaneous experimental OH-PLIF signals (left) and OH mass fractions of the LES (right). In both the experiments and the LES, the OH profile suggest a scattered and dynamic behaviour of the flame. This strongly indicates a fragmented flame, with pockets of high values next to regions with almost no OH. The images from the LES show that this scattered OH behaviour continues downstream of the combustor, although the highest concentration pockets are mainly located upstream and above the cavity. There are some notable differences between the experimental and LES results, with the LES showing OH pockets much closer to the injector and occurring over the full height of the combustor in these regions, while the experimental results show OH primarily along the lower surface of the jet. The LES results show a highly dynamic flame behaviour that is not obvious in the experimental results presented, though it is unclear from [6].

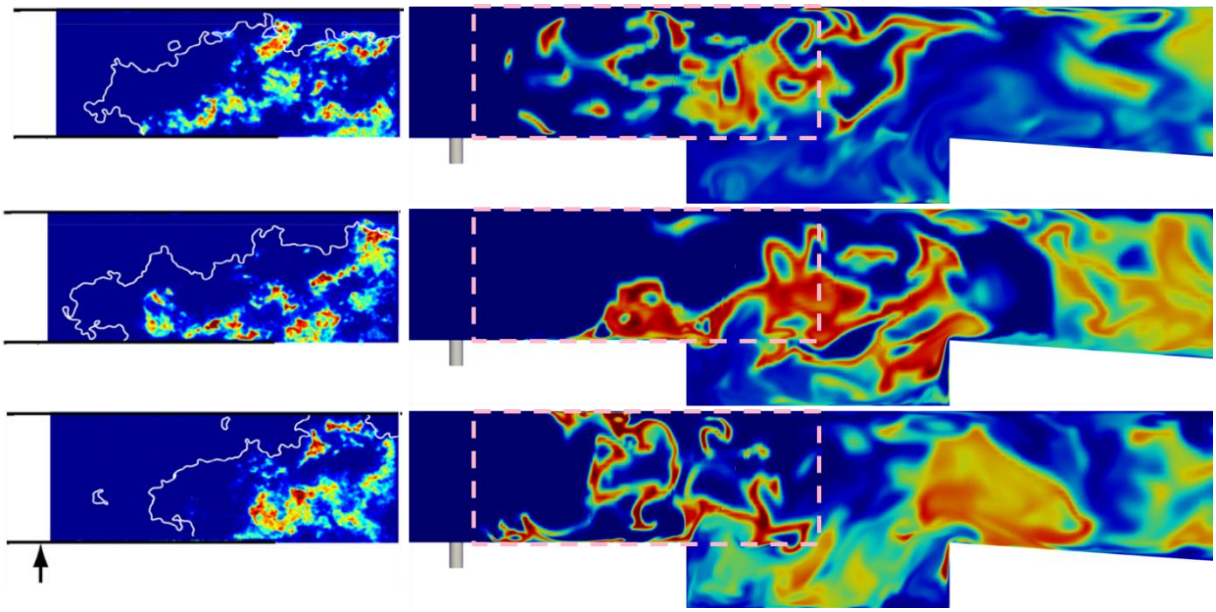

Figure 10. Simultaneous instantaneous $CH_2O$ and OH-PLIF images from experiments on the left, and instantaneous OH mass fraction from simulations on the right. The $CH_2O$ is marked with the white outline in the experiments, left. The pink boxes in the simulations indicates the location of the images in the experiments. The experiments are made at slightly lower air static temperatures (1364 K instead of 1390 K).

## 5.2 Dynamic Combustor Behavior

To illustrate the dynamic features of the combustion in the LES, five snapshot images of the temperature, visualized using volumetric rendering, are shown in Figure 11. These images show how the flame goes from a cavity-stabilized case, t=5.7 µs, moving to a jet-wake stabilized case, t=6.7 µs, and then back to being cavity stabilized again, t=7.7 µs. This sequence occurs twice in the five snapshots and the flame oscillates between the extremes of being almost extinguished (t=9.5 µs) to filling the whole height of the combustor (t=6.7 µs and 8.7 µs), causing thermal choking.

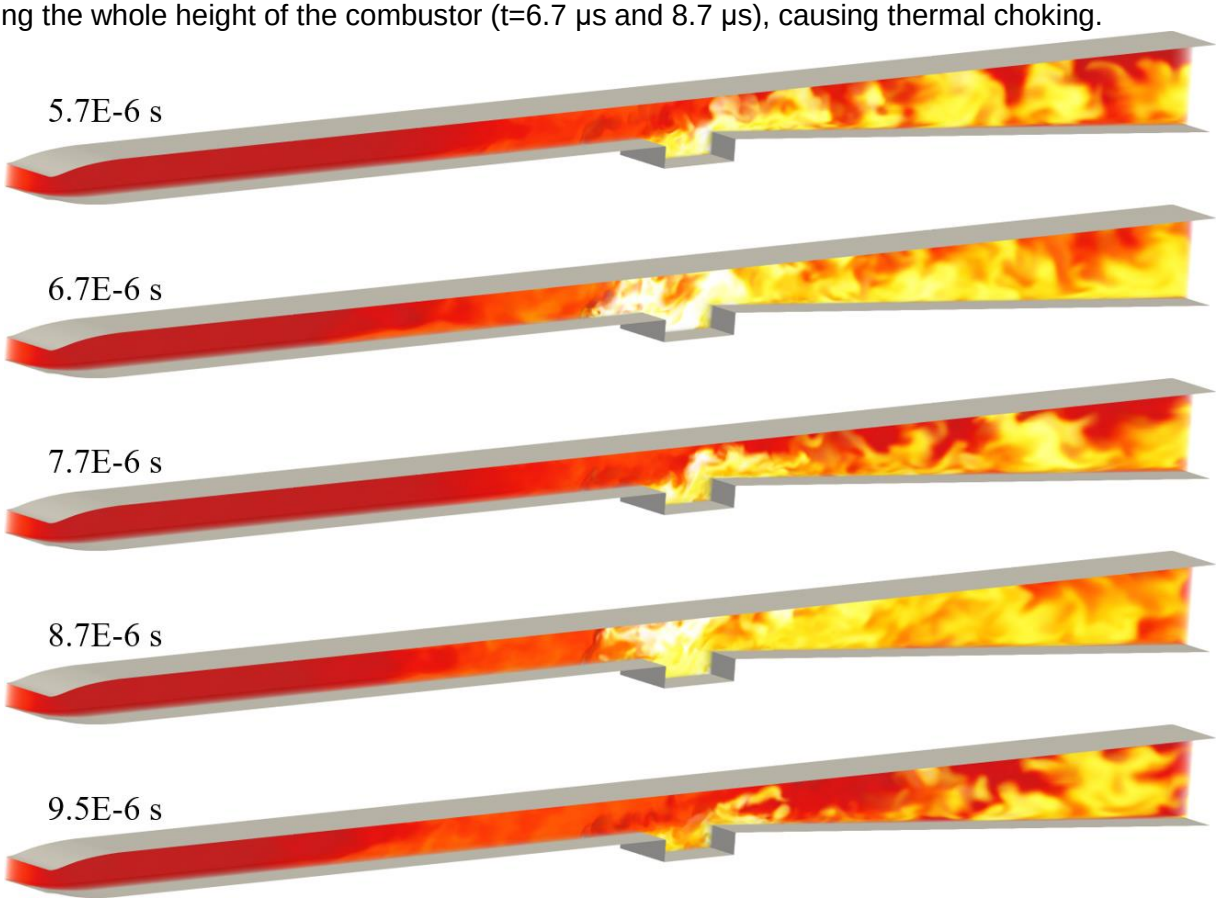


Figure 11 - Volumetric rendered temperature, shown at five different times to illustrate the highly dynamic behavior of the flame.

To further investigate the inherent flame characteristics, volume-renderings of the combustion heat release ($\dot{Q}$) and mass fractions of $C_2H_2$, CH and OH are plotted for the two extreme flame positions: a thermally-choked jet-wake stabilized flame, Figure 12, and an almost quenched, cavity-stabilized, flame, Figure 13. $C_2H_2$ is chosen since it is an early $C_2$ intermediate specie, produced through H-abstraction, via H or OH radicals, of the initial fuel breakdown product $C_2H_3$. $C_2H_2$ therefore represents a species early in the carbon oxidation chain, a chain that will eventually end in CO and $CO_2$ formation. CH on the other hand represents one of the later steps in the carbon oxidation chain, is produced from $C_2H$ or $CH_2$, and is also one of the measured species. Finally, OH is shown since it represents the post-flame region [55] and it is one of the measured species.

Figure 12, showing a thermally choked condition at t=6.7 µs, has a clear jet-wake stabilized flame, with a high heat release positioned closely behind the fuel inlet plume. Both carbon species are present and oxidized in the region of high heat release, and are non-existent further downstream of the combustor. This shows that the reaction sequence for the carbonated species, going from $C_2H_4$ to $CO_2$, has transitioned through both $C_2H_2$ and CH species in a short time (and hence distance) at these high temperatures.

The OH plots show high values in the areas of high heat release but OH is also present further downstream, a consequence of its post-flame nature and the fact that the temperature is high in large parts downstream of the cavity, effectively promoting OH production.


Figure 12 - Volumetric rendered temperature, heat release, $C_2H_2$, CH and OH along the centerline of the x-axis, at an instant where the flame is jet-wake stabilized.

At a cavity stabilized condition, at t=9.5 µs shown in Figure 13, many differences can be seen in comparison to the thermally choked case. Apart from the obvious differences in the temperature magnitude and distribution, the chemical heat release $\dot{Q}$ is distributed over a wider region downstream of the cavity and has lower peak amplitude. This demonstrates a less intense combustion, extending from its core in the cavity all the way to the outlet. The $C_2H_2$ profile is also markedly different, with relatively high values in the majority of the combustor behind the fuel inlet plume all the way to the outlet, indicating non-complete combustion. A large part of the carbon chain has therefore only progressed from $C_2H_4$ to $C_2H_2$ with low values in CH indicating that only a minor fraction of the fuel (and $C_2H_2$) has oxidized far enough down the carbon chain for CH to exist. This stand in stark contrast

to the thermally choked case in Figure 12 where the low values of CH are a consequence of more or less complete combustion where the carbon chain had progressed past both $C_2H_2$ and CH.

The OH distribution in the cavity stabilized case shows significantly lower peak value and distribution compared to the thermally choked case. As in the thermally choked case, the OH distribution follows that of the high temperatures very closely.

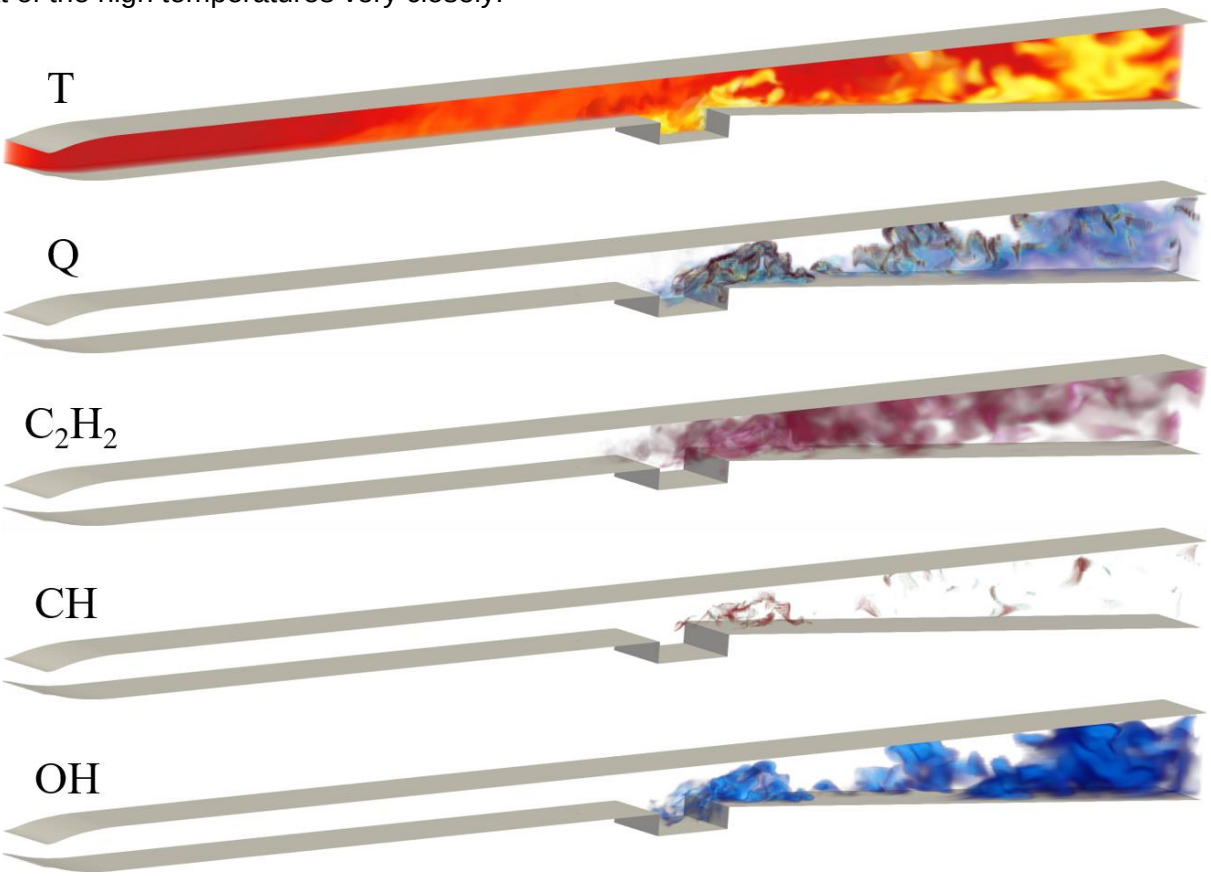


Figure 13 - Volumetric rendered temperature, heat release, $C_2H_2$, CH and OH along the centerline of the x-axis, at an instant where the flame is cavity stabilized.

The close investigation of the heat release and species distributions of the two extremes shown in Figures 12 and 13 helps explaining some of the underlying chemical responses to the different flame conditions.

Figure 14 shows volume-renderings of the time-averaged temperature and fluctuations. Although the highest temperatures can occasionally be present just behind the fuel inlet plume, as seen in Figure 11, the temperature is most consistently high within the cavity. This shows the importance of the cavity as a ‘heat reservoir’ in the combustor with an important role in flame stabilization. Note the slightly lower mean temperature in a wedge-shaped part just behind the cavity.

The temperature fluctuation plot shows that these are highest above the second half of the cavity, matching the location of the CH mean peak in Figure 8. The temperature fluctuations however also show a slightly extended medium values right up to the fuel inlet plume, a consequence of the frequent changes in flame position, and their corresponding thermally choked conditions, upstream of the combustor, as indicated in Figure 11.

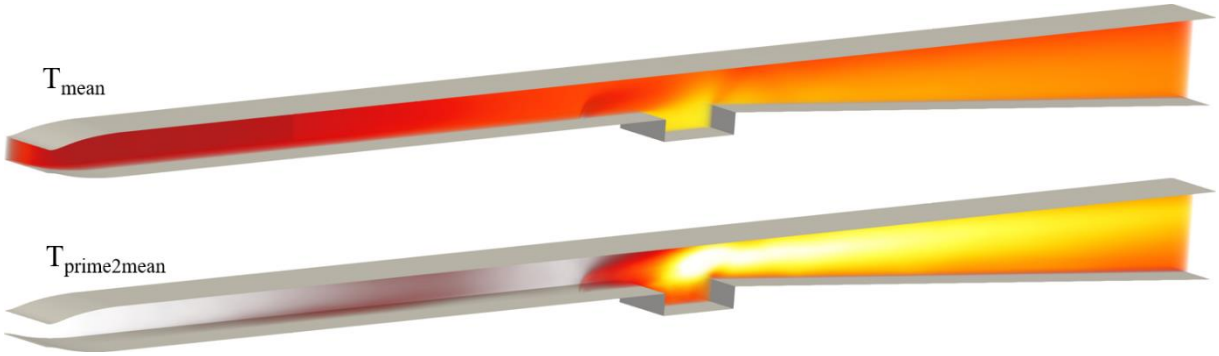


Figure 14 - Volumetric rendered mean temperature (top) and temperature fluctuations (bottom), along the centerline of the x-axis.

The corresponding mean and fluctuation plots for the heat release, Figure 15, show that these quantities are centred above the cavity. As shown in Figure 15(a), the distribution of the mean heat release closely matches that of the mean CH density, Figure 8. The fluctuations however show one large region above the cavity and one smaller just behind the fuel inlet plume. The latter is an effect of the unsteady behaviour with its occasional jet-wake stabilized flame position indicated in Figure 11 at t=6.7e-6 and 8.7e-6 s, and Figure 15 clearly showing the upstream positioning of the heat release.

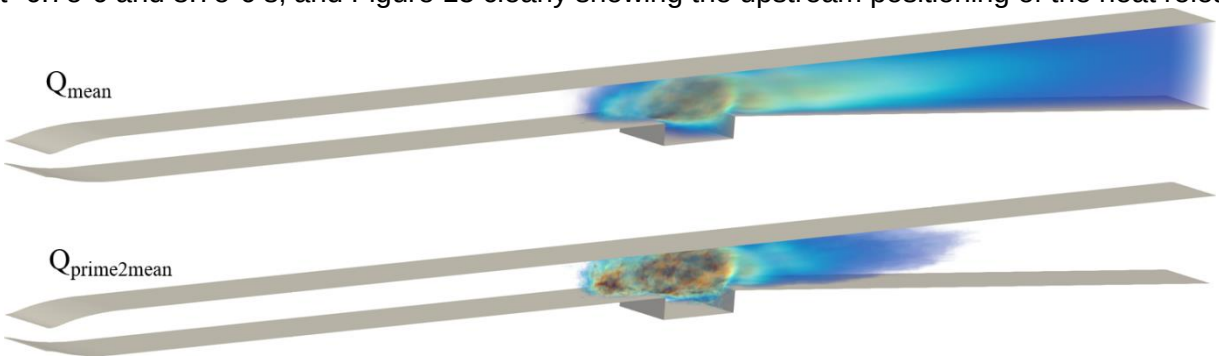


Figure 15 - Volumetric rendered mean heat release (top) and heat release fluctuations (bottom), along the centerline of the x-axis.

In order to further study the one-dimensional dynamics along the length of the combustor, the whole domain has been divided into 400 equally sized sections along the combustor. By integrating or averaging combustion fields such as temperature, pressure, heat release and individual species fractions within each section as appropriate, the data is reduced to a one-dimensional profile. This reduction is performed at regular time intervals during the simulation, allowing for x-t plots of the variables to be generated, exemplified for the temperature in Figure 16. The elapsed time is on the y-axis and the distance along the combustor on the x-axis, with the colouring representing the magnitude of the presented quantity.

From the x-t plots presented in Figure 16, a clear periodic one-dimensional behaviour can be seen, with a period of between 3 and 6 ms. Each period is characterised by periods of intense heat release, initially over the cavity and then propagating upstream toward the fuel injector. As the intense combustion region grows, it causes increased choking of the flow, resulting in the propagation of a higher-pressure and -temperature region upstream into the isolator. As a result of this increased choking, air flow past the injector decreases markedly, combustion is reduced, and the ignition point moves back towards the rear of the cavity. This in turn reduces the choking again, allowing the air flow to increase, and the cycle restarts. The flame hence oscillates between a cavity-based mode to jet-wake mode, and never stabilizes in either position for a longer period. Note that for some cycles there are also time intervals for which the flame is near extinguished, before reigniting again around the rear of the cavity. These intervals correspond closely to those times when the high pressure and temperature region extends furthest into the isolator.

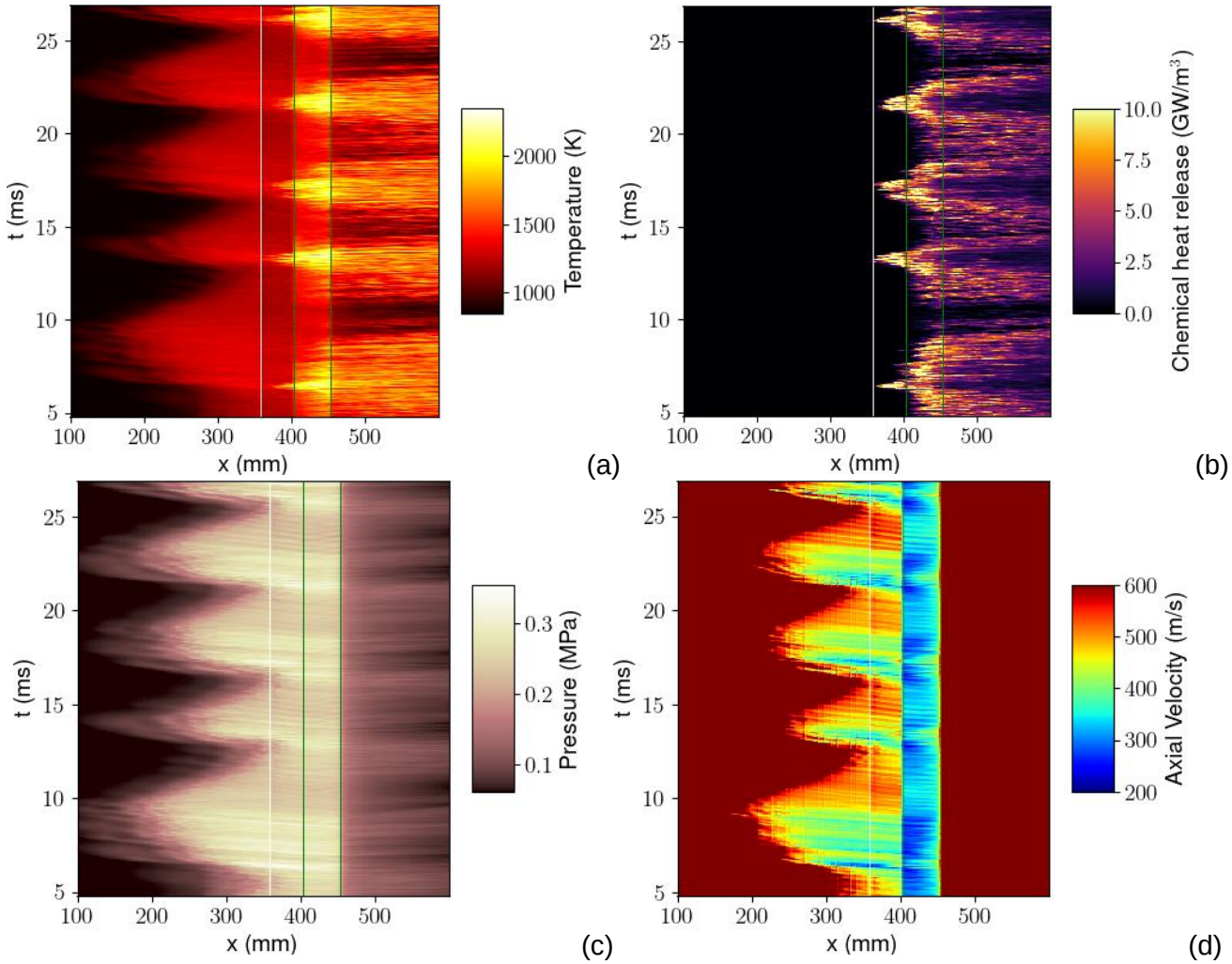


Figure 16 – One-dimensional (a) temperature, (b) chemical heat-release, (c) pressure and (d) axial velocity profiles computed by volume averaging in cross-sectional slabs along the combustor length, plotted over time. Note colour-scale for velocity plot is capped to 600 m/s to focus on near-injector region. White line indicates fuel-injector position, green lines indicate cavity extent.

In order to try and examine the coupling of the chemical kinetics to the temperature bursts and their resulting acceleration of the flame to the jet-wake position, similar x-t plots where made for all 23 species involved. One species emerged as a possible pre-cursor for these semi-regular temperature bursts, $H_2O_2$, shown in Figure 17. There is a negative correlation between the locations of species and the temperature, Figure 16(a), with $H_2O_2$ present in high concentrations when the temperature is low and vice versa. Almost all other species show a positive correlation with the temperature field. The reason for this is that at times when the flame is jet-wake stabilized its temperature is higher, minimizing the low-temperature $H_2O_2$ reaction routes.

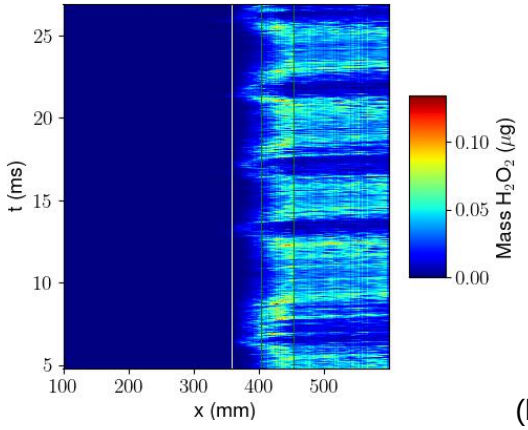


Figure 17 - One-dimensional $H_2O_2$ profile computed by integration over cross-sectional slabs along combustor length, plotted over time.

To investigate further the behaviour of $H_2O_2$, a zero-dimensional constant volume simulation was performed at an initial temperature of 1000 K, matching the low-temperature regions in the combustor. This simulation was repeated using both $C_2H_4$-air and 50/50 $C_2H_4$-$H_2$-air mixtures in order to identify differences due to additional $H_2$ in the fuel. The results, plotted in Figure 18, clearly show that the temperature increase occurs slightly faster with $H_2$ enrichment (dashed lines), in agreement with the ignition delay time results in Figures 6(a) and 6(b).
Figure 18 clearly shows a build-up of $H_2O_2$ ahead of the thermal runaway. The $H_2O_2$ curve shapes are also different depending on whether the fuel is $H_2$ enriched or not (green dashed versus solid lines). $H_2O_2$ with $H_2$ enrichment shows clear build-up ahead of the flame, both in the LES and in this zero-dimensional simulation, and this build-up gets stronger with added $H_2$ in the fuel mixture. All this suggests that tracking $H_2O_2$ enables one to forecast the irregular behaviour present in this case.

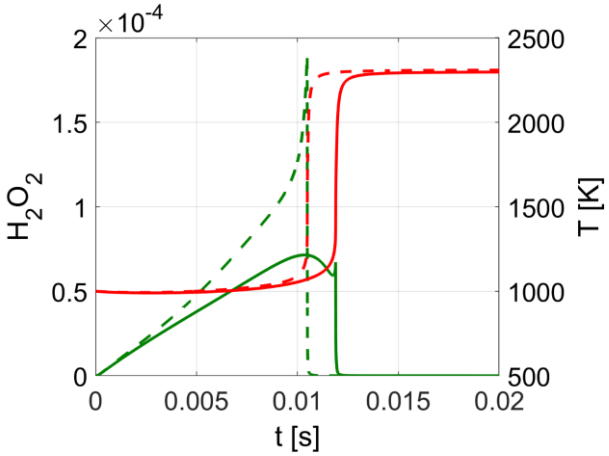


Figure 18 - Simulation results of a zero-dimensional constant volume set-up, with an initial temperature of 1000 K. Results from both $C_2H_4$-air (solid lines) and 50/50 $C_2H_4$-$H_2$-air (dashed lines) mixtures are shown, with the temperature in red on the right y-axis and $H_2O_2$ on the left y-axis.

Finally, Figure 19 show the volumetric averaging of the pressure, p, and the integrated heat release, $\dot{Q}$, over the complete domain. The high-frequency fluctuations in the heat release show the highly dynamic, while the moving average reveals the lower-frequency periodic behaviour identified in the previous section. Comparison of the pressure and heat release moving averages reveals a phase-shift between the two signals, with the pressure fluctuations lagging the heat release by 1 to 2 ms.

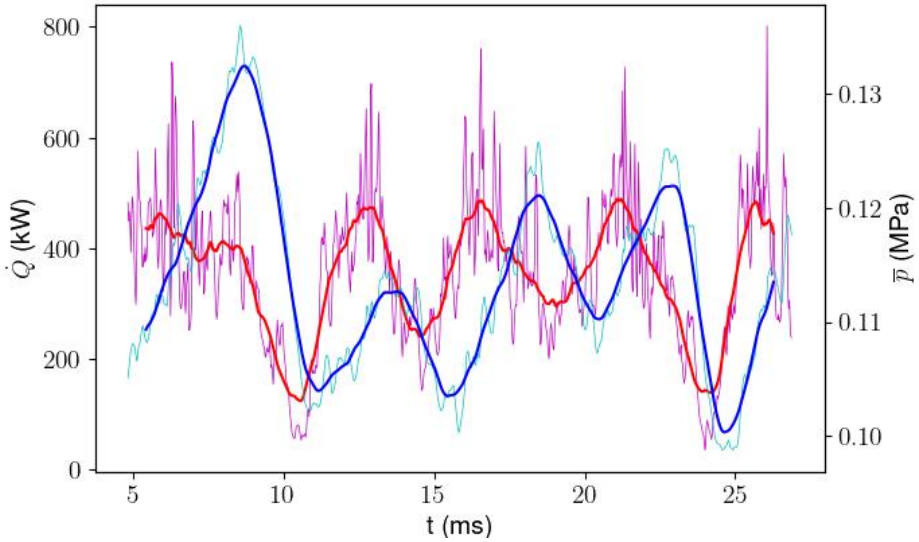


Figure 19 - Volumetric averaging of pressure, *p*, and integrated heat release, $\dot{Q}$, over the whole combustor. Instantaneous $\dot{Q}$ in pink, moving average of $\dot{Q}$ in red, Instantaneous *p* in light blue, moving average of *p* in blue.

## 6. Concluding Remark

An ethylene-hydrogen fueled ramjet engine rig has been simulated using combustion LES with finite-rate chemistry using a 66-step reaction mechanism. Comparisons have been made for key experimental data such as CH-PLIF and OH-PLIF, with generally good agreement between the time-averaged experiment results and the simulation. The simulation shows a highly dynamic flame behavior, where the flame anchoring moves constantly between the cavity and the jet-wake. The intense combustion associated with the flame moving to jet-wake anchoring is accompanied by thermal choking, which effectively terminates the condition where the flame can be sustained in the jet-wake position and the flame decreases in size and moves back to a cavity stabilized position. Unfortunately no experimental data is currently available to corroborate the dynamic flame behavior seen in the simulation, but the simulation results strongly resemble the behaviour seen for the previously studied pure hydrogen case [52].

One way of trying to predict the transition of the flame anchoring to the jet-wake is to identify key species that accumulate before such an event in time. A suitable species identified here is $H_2O_2$, with $H_2O_2$ shown to accumulate in and behind the cavity well before the intense combustion periods and subsequent acceleration of the flame to the jet-wake state. Right in between two states of jet-wake stabilization the $H_2O_2$ is at a relatively constant level, and its accumulation is accelerated as it towards the transition into a jet-wake state. The accumulation of $H_2O_2$ ahead of the highest temperature gradient was demonstrated constant volume simulations, where the accumulation is stronger for an ethylene-hydrogen case compared to a pure hydrogen one.

It is shown that the LES is capable, when sufficiently detailed chemical kinetic modelling is used, to capture highly dynamic flame behavior, and that the current simulation matches the experimental data available for the case studied.

## 7. Copyright Statement



## References

[1] Saghafian, A., Shunn, L., Philips, D. A., & Ham, F. Large Eddy Simulations of the HIFiRE Scramjet using a Compressible Flamelet/Progress Variable Approach. *Proc Combust Inst.*, Vol. 35, pp 2163, 2015.

[2] Potturi, A. S., & Edwards, J. R. Large-eddy/Reynolds-averaged Navier–Stokes simulation of cavity-stabilized ethylene combustion. *Combust Flame*, Vol. 162, No., 4, pp 1176–92, 2015.

[3] Weixin, D., Jialing, L., Shunhua, Y., Ye, T., Wanzhou, Z., & Mingheng, X. Ethylene fueled scramjet combustion experiments. *Mod Appl Sci.*, Vol. 77, No. 5, pp 51, 2013.

[4] Boles, J., Edwards, J., Choi, J. I., & Baurle, R. Simulations of high-speed internal flows using LES/RANS models. *47th AIAA Aerospace Sciences Meeting including The New Horizons Forum and Aerospace Exposition*, Orlando, Florida, USA, pp 1324, 2009.

[5] Choi, J., & Menon, S. Large-Eddy Simulation of cavity-stabilized supersonic combustion. *45th AIAA/ASME/SAE/ASEE Joint Propulsion Conference & Exhibit*, Denver, Colorado, USA, pp 5383, 2009.

[6] Micka, D. J., & Driscoll, J. F. Stratified jet flames in a heated (1390 K) air cross-flow with autoignition. *Combust Flame*. Vol. 159, No. 3, pp 1205–14, 2012.

[7] Micka, D., & Driscoll, J. Reaction zone imaging in a dual-mode scramjet combustor using CH-PLIF. *44th AIAA/ASME/SAE/ASEE joint propulsion conference & exhibit*, Hartford, CT, USA, pp 5071, 2008.

[8] Liu, B., He, G. Q., & Qin, F. Simulation of supersonic Ethylene–Hydrogen and air auto-ignition flame using skeletal mechanism. *Acta Astronaut.*,Vol. 152, pp 521–33, 2018.

[9] Zhong, F., Cheng, L., Gu, H., & Zhang, X. Experimental study of flame characteristics of ethylene and its mixture with methane and hydrogen in supersonic combustor. *Aerosp Sci Technol.*,Vol. 86, pp 775–81, 2019.

[10] Hass, N., Cabell, K., Storch, A., & Gruber, M. HIFiRE direct-connect rig (HDCR) phase I scramjet test results from the NASA Langley arc-heated scramjet test facility. In San Fransisco, CA, USA,. pp 2248, 2011.

[11] Bermejo-Moreno, I., Larsson, J., Bodart, J., Vicquelin, R. Wall-modeled large-eddy simulations of the HIFiRE-2 scramjet. *Center for Turbulence Research*, Report No.: hal-1780950, 2013.

[12] Yao, W., Wang, J., Lu, Y., Li, X., & Fan, X. Full-scale Detached Eddy Simulation of kerosene fueled

scramjet combustor based on skeletal mechanism. *20th AIAA International Space Planes and Hypersonic Systems and Technologies Conference*, Glasgow, Scotland, pp 3579, 2015.

[13] Yu, G., Li, J. G., Zhao, J. R., Yue, L. J., Chang, X. Y., & Sung, C. J. An experimental study of kerosene combustion in a supersonic model combustor using effervescent atomization. *Proc Combust Inst.* Vol. 30, No. 2, pp 2859–66, 2005.

[14] Bao, W., Hu, J., Zong, Y., Yang, Q., Wu, M., Chang, J., & Yu, D. Combustion characteristic using O2-pilot strut in a liquid-kerosene-fueled strut-based dual-mode scramjet. *J Aerosp Eng.* Vol. 227 No. 12, pp 1870–80, 2013.

[15] Zhang, M., Hu, Z., He, G., & Liu, P. Large-eddy simulation of kerosene spray combustion in a model scramjet chamber. *J Aerosp Eng.* Vol. 224, No. 9, pp949–60, 2010.

[16] Tian, Y., Yang, S., Le, J., Zhong, F., & Tian, X. Investigation of the effects of fuel injector locations on ignition and flame stabilization in a kerosene fueled scramjet combustor. *Aerosp Sci Technol.* Vol. 70, pp 310–316, 2017.

[17] Yu, G., Li, J. G., Chang, X. Y., Chen, L. H., & Sung, C. J. Investigation of kerosene combustion characteristics with pilot hydrogen in model supersonic combustors. *J Propuls Power.* Vol. 17 No. 6, pp 1263–72, 2001.

[18] Menon S. & Fureby C. Computational Combustion. *Encyclopedia of Aerospace Engineering*. John Wiley & Sons; 2010.

[19] Pitsch, H. Large-eddy simulation of turbulent combustion. *Annu Rev Fluid Mech.* Vol. 38, pp 453–82, 2006.

[20] Micka, D. J. Combustion stabilization, structure, and spreading in a laboratory dual-mode scramjet combustor, *Doctoral Dissertation*, Michigan, USA, University of Michigan, 2010.

[21] Micka, D. J., & Driscoll, J. F. Combustion characteristics of a dual-mode scramjet combustor with cavity flameholder. *Proc Combust Inst*. Vol. 3, No. 2, pp 2397–404, 2009.

[22] Driscoll J.F. & Rasmussen C.C. Correlation and Analysis of Blowout Limits of Flames in Highspeed Airflows. *J Propuls Power.* Vol. 21, pp 1035, 2005.

[23] Gruber M.R., Donbar J.R, Carter C.D. & Hsu K.-Y. Mixing and Combustion Studies using Cavity-based Flameholders in a Supersonic Flow. *J Propuls Power.* Vol. 20, pp 769, 2004.

[24] Rasmussen C.C., Dhanuka S.K. & Driscoll J.F. Visualization of Flameholding Mechanisms in a Supersonic Combustor using PLIF. *Proc Combust Inst.* Vol. 31:pp 2505, 2007.

[25] Echekki T. & Mastorakos E. *Turbulent Combustion: Concepts, Governing Equations and Modeling Strategies,* in Turbulent Combustion Modeling: Advances, New Trends and Perspectives. Netherlands: Springer; 2011.

[26] Fureby, C. Large eddy simulation modelling of combustion for propulsion applications. *Philos Trans R Soc Math Phys Eng Sci.* Vol. 367, No. 1899, pp 2957–69, 2009.

[27] Nogenmyr, K. J., Fureby, C., Bai, X. S., Petersson, P., Collin, R., & Linne, M. Large eddy simulation and laser diagnostic studies on a low swirl stratified premixed flame. *Combust Flame*. Vol. 156, No. 1, pp 25–36, 2009.

[28] Fedina, E., & Fureby, C. A comparative study of flamelet and finite rate chemistry LES for an axisymmetric dump combustor. *J Turbul.* Vol. 12, No. N24, 2011.

[29] Zettervall, N., Nordin-Bates, K., Nilsson, E. J. K., & Fureby, C. Large Eddy Simulation of a premixed bluff body stabilized flame using global and skeletal reaction mechanisms. *Combust Flame.* Vol. 179, pp 1–22, 2017.

[30] Fedina, E., Fureby, C., Bulat, G., & Meier, W. Assessment of finite rate chemistry large eddy simulation combustion models. *Flow Turbul Combust.* Vol. 99, No. 2, pp 385–409, 2017.

[31] Fureby, C., Nordin-Bates, K., Petterson, K., Bresson, A., & Sabelnikov, V. A computational study of supersonic combustion in strut injector and hypermixer flow fields. *Proc Combust Inst.* Vol. 35, No. 2, pp 2127–35, 2015.

[32] Nordin-Bates, K., & Fureby, C. Understanding scramjet combustion using LES of the HyShot II combustor: stable combustion and incipient thermal choking. *51st AIAA/SAE/ASEE Joint Propulsion Conference*, Orlando, FL, pp 3838, 2015.

[33] Weller H.G., Tabor G., Jasak H. & Fureby C. A Tensorial Approach to CFD using Object Oriented Techniques. *Comput Phys.* Vol. 12, No. 6, pp 620–31, 1997.

[34] Grinstein, F. F., Margolin, L. G., & Rider, W. J. *Implicit large eddy simulation. Vol. 10*. Cambridge: Cambridge university press; 2007.

[35] Hairer, E., Wanner, G., & Solving, O. D. E. *II: Stiff and Differential-Algebraic Problems*. Berlin: Springer; 1991.

[36] Zettervall, N., Fureby, C., & Nilsson, E. J. K. Small Skeletal Kinetic Reaction Mechanism for Ethylene–Air Combustion. *Energy Fuels.* Vol. 31, No. 12, pp 14138–49, 2017.

[37] Metcalfe, W. K., Burke, S. M., Ahmed, S. S., & Curran, H. J. A Hierarchical and Comparative Kinetic Modeling Study of C1− C2 Hydrocarbon and Oxygenated Fuels. *Int J Chem Kinet.* Vol. 45, pp 638, 2013.

[38] "Chemical-Kinetic Mechanisms for Combustion Applications", San Diego Mechanism web page, Mechanical and Aerospace Engineering (Combustion Research), *University of California at San Diego.* http://combustion.ucsd.edu.

[39] *USC mechanism website*, accessed 2020. http://ignis.usc.edu/Mechanisms/USC-Mech%20II/USC_Mech%20II.htm.

[40] Zettervall, N., Fureby, C., & Nilsson, E. J. K. Small skeletal kinetic mechanism for kerosene combustion. *Energy Fuels.* Vol. 30, No. 11, pp 9801–13, 2016.

[41] Zettervall, N., Fureby, C., & Nilsson, E. J. K. A reduced chemical kinetic reaction mechanism for kerosene-air combustion. *Fuel*. Vol. 269, pp 117446, 2020.

[42] Zettervall, N., Worth, N. A., Mazur, M., Dawson, J. R., & Fureby, C. Large eddy simulation of CH4-air and C2H4-air combustion in a model annular gas turbine combustor. *Proceedings of the Combustion Institute*. Dublin, pp 5223–31, 2019.

[43] Danel, K., Zettervall, N., & Fureby, C. A Combined Experimental and Computational Study of Jet Engine Combustion–Baseline Engine Operation, *AIAA Propulsion and Energy Forum*, Indianapolis, Indiana, USA, pp 4328, 2019.

[44] Jomaas, G., Zheng, X. L., Zhu, D. L., & Law, C. K. Experimental Determination of Counterflow Ignition Temperatures and Laminar Flame Speeds of C2–C3 Hydrocarbons at Atmospheric and Elevated Pressures. *Proc Combust Inst.* Vol. 30, No. 1, pp 193–200, 2005.

[45] Kochar, Y., Seitzman, J., Lieuwen, T., Metcalfe, W., Burke, S., Curran, H., ... & Bourque, G. Laminar Flame Speed Measurements and Modeling of Alkane Blends at Elevated Pressures with Various Diluents. *ASME 2011 Turbo Expo: Turbine Technical Conf and Exposition*, Vancouver, British Colombia, Canada, pp 129–40, 2011.

[46] Egolfopoulos, F. N., Zhu, D. L., & Law, C. K. Experimental and numerical determination of laminar flame speeds: mixtures of C2-hydrocarbons with oxygen and nitrogen. pp 471–8, Elsevier, 1991.

[47] Hassan, M. I., Aung, K. T., Kwon, O. C., & Faeth, G. M. Properties of Laminar Premixed Hydrocarbon/Air Flames at Various Pressures. *J Propuls Power.* Vol. 14, pp 479, 1998.

[48] Mathieu, O., Goulier, J., Gourmel, F., Mannan, M. S., Chaumeix, N., & Petersen, E. L. Experimental study of the effect of CF3I addition on the ignition delay time and laminar flame speed of methane, ethylene, and propane. *Proc Combust Inst.* Vol. 35, No. 3, pp 2731–9, 2015.

[49] Law, C. K., Makino, A., & Lu, T. F. On the off-stoichiometric peaking of adiabatic flame temperature with equivalence ratio. *The 4th Joint Meeting of the US Sections of the Combustion Institute*. Philadelphia, PA, USA; 2005.

[50] Kopp, M. M., Donato, N. S., Petersen, E. L., Metcalfe, W. K., Burke, S. M., & Curran, H. J. Oxidation of Ethylene–Air Mixtures at Elevated Pressures, Part 1: Experimental Results. *J Propuls Power.* Vol. 30, pp 790, 2014.

[51] Kalitan, D. M., Hall, J. M., & Petersen, E. L. Ignition and oxidation of ethylene-oxygen-diluent mixtures with and without silane. *J Propuls Power.* Vol. 21, No. 6, pp 1045–56, 2005.

[52] Zettervall, N., & Fureby, C. A Computational Study of Ramjet, Scramjet and Dual-mode Ramjet Combustion in Combustor with a Cavity Flameholder. *2018 AIAA Aerospace Sciences Meeting*, Kissimmee, Florida, USA, 2018. p. 1146, 2018.

[53] Saxena, S., Kahandawala, M. S. P., & Sidhu, S. S. A shock tube study of ignition delay in the combustion of ethylene. *Combust Flame.* Vol. 158, No. 6, pp1019–31, 2011.

[54] Kumar, K., Mittal, G., Sung, C. J., & Law, C. K. An experimental investigation of ethylene/O2/diluent mixtures: Laminar flame speeds with preheat and ignition delays at high pressures. *Combust Flame.* Vol. 153, No. 3, pp 343–54, 2008.

[55] Glassman I, Yetter RA. *Combustion*. 4th ed. Elsevier; 2010.